ELSEVIER

International Journal of Solids and Structures 41 (2004) 1061–1080

INTERNATIONAL JOURNAL OF SOLIDS and STRUCTURES

www.elsevier.com/locate/ijsolstr

Numerical analysis of prestressed concrete beams using a coupled element free Galerkin/finite element approach

T. Rabczuk [a,b,*], J. Eibl [b]

[a] Department of Mechanical Engineering, Northwestern University, 2145 N Sheridan Road, Evanston, IL 60208-311, USA
[b] Institute of Concrete Structures and Building Materials, University of Karlsruhe 76128, Germany

Received 1 December 2002; received in revised form 27 July 2003

Abstract

The topic of this paper is the analysis of prestressed concrete beams under quasistatic loading. Therefore, a coupled element free Galerkin finite element approach is chosen. The concrete is modeled with particles and the reinforcement with beam elements. For the steel, an elastoplastic constitutive law with isotropic hardening and a tension cutoff is applied. The concrete is modeled via a continuum damage model, where an anisotropic tensile damage variable is used to capture the appropriate behavior of concrete in tension. Since the interaction between the concrete and the reinforcement is crucial, the bond behavior cannot be ignored. The relative displacements between the reinforcement and the adjacent concrete particles are calculated. The resulting bond forces tangential and normal to the reinforcement are applied onto the elements and the adjacent concrete particles. The numerical results are compared with two experiments with different failure mechanisms and agree well.
© 2003 Elsevier Ltd. All rights reserved.

1. Introduction

For the development of an uniform European norm, the behavior of prestressed concrete beams became of interest, especially for those without stirrup reinforcement. In this article we present a technique to study the behavior of such beams within the framework of a numerical analysis. Other approaches for analyzing and designing prestressed concrete structures are given by Liang et al. (2001, 2002). The problem is treated in two dimensions (plane stress). Hereby, the initiation and propagation of cracks in concrete is crucial. Since finite element (FE) and finite difference methods (FDM) have had difficulties in modeling cracks, we choose a meshfree method, the element free Galerkin (EFG) method with nodal integration (see Beissel and Belytschko, 1996), and an explicit time integration scheme. EFG with nodal integration is similar to the moving least square particle hydrodynamics (MLSPH) method (see Dilts, 1999) which is an improvement of the smooth particle hydrodynamics (SPH) method developed by Lucy (1977) and Gingold and

* Corresponding author. Address: Department of Mechanical Engineering, Northwestern University, 2145 N Sheridan Road, Evanston, IL 60208-311, USA. Tel.: +1-847-4913046; fax: +1-847-4913915.
E-mail address: t-rabczuk@northwestern.edu (T. Rabczuk).

0020-7683/$ - see front matter © 2003 Elsevier Ltd. All rights reserved.
doi:10.1016/j.ijsolstr.2003.09.040

Monaghan (1977). We prefer a meshfree approach instead of finite elements because meshfree methods are better suitable to describe continuum models in many aspects as isotropy, smoothness, continuity, nonlocal character in interpolation, flexible connectivity and adaptive refinement (see also Belytschko and Lu, 1995; Belytschko et al., 1996a,b; Liu et al., 1995, 1996b and Liu et al., 1996a). Especially in crack propagation problems where finite elements are bounded to a specific topology, computational expensive remeshing algorithms become necessary. Adaptive refinement approaches can easily be incorporated in meshfree methods which make meshfree methods attractive for this class of problems.

A combined damage plasticity constitutive law is applied, which models the anisotropy of concrete in tension by a damage vector. The crack is represented by a damage zone. As shown later, it is sufficient enough to reproduce the essential failure mechanisms observed in experiments. The reinforcement is treated with beam elements and an elastoplastic model with a strain based tension cutoff, so that the failure of the reinforcement can be captured, too. In some experiments, especially when the beam is loaded close to its support, an anchorage failure was observed in the experiments. Therefore, the bond model becomes crucial. A procedure is proposed to describe the interaction of the reinforcement with the concrete particles. Finally, our numerical results are compared with the results of two experiments with different failure mechanisms. We show, that our model is able to capture the substantial failure mechanisms although improvements are desirable in certain cases.

2. The constitutive model for concrete

The constitutive law for concrete is a coupled damage-plasticity model as proposed by Schmidt-Hurtienne (2001). According to Fig. 1, the strain rate tensor $\dot{\boldsymbol{\epsilon}}$ is decomposed in an elastic $\dot{\boldsymbol{\epsilon}}_{\mathrm{e}}$, a damage $\dot{\boldsymbol{\epsilon}}_{\mathrm{d}}$ and a plastic part $\dot{\boldsymbol{\epsilon}}_{\mathrm{p}}$. The rate equations for strains and stresses are given by

$$\dot{\boldsymbol{\epsilon}} = \dot{\boldsymbol{\epsilon}}_{\mathrm{e}} + \dot{\boldsymbol{\epsilon}}_{\mathrm{d}} + \dot{\boldsymbol{\epsilon}}_{\mathrm{p}} = \dot{\boldsymbol{\epsilon}}_{\mathrm{ed}} + \dot{\boldsymbol{\epsilon}}_{\mathrm{p}} \tag{1}$$

$$\boldsymbol{\sigma}_{\mathrm{e}}^{\nabla} - \boldsymbol{\sigma}^{\nabla} = \mathbf{E} : \dot{\boldsymbol{\epsilon}} - \mathbf{E} : \dot{\boldsymbol{\epsilon}}_{\mathrm{e}} = -\boldsymbol{\sigma}_{\mathrm{d}}^{\nabla} - \boldsymbol{\sigma}_{\mathrm{p}}^{\nabla} = \mathbf{E} : \dot{\boldsymbol{\epsilon}}_{\mathrm{d}} + \mathbf{E} : \dot{\boldsymbol{\epsilon}}_{\mathrm{p}} \tag{2}$$

where the elastic and the damage strain rate is combined to $\dot{\boldsymbol{\epsilon}}_{\mathrm{ed}}$ and $\boldsymbol{\sigma}^{\nabla}$, $\boldsymbol{\sigma}_{\mathrm{e}}^{\nabla}$, $\boldsymbol{\sigma}_{\mathrm{d}}^{\nabla}$ and $\boldsymbol{\sigma}_{\mathrm{p}}^{\nabla}$ are frame indifferent stress rates.

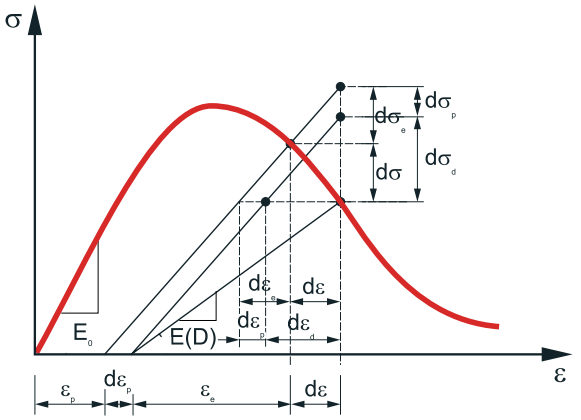

Fig. 1. The constitutive law for concrete.

The damage loading surface $F_d = F_d[\epsilon_e, \kappa_d] = 0$ is formulated in the strain space and is decoupled from the plasticity loading surface $F_p = F_p[\epsilon, \kappa_p] = 0$, where κ_d is the equivalent damage strain of the elastic strain tensor ϵ_e and κ_p the equivalent plastic strain. In contrast to the usual theory, the plastic flow rule does not determine the relaxation stress $\dot{\boldsymbol{\sigma}}_p$ but directly the plastic strain increment $\dot{\boldsymbol{\epsilon}}_p$

$$\dot{\boldsymbol{\epsilon}}_p = \dot{\lambda}_p \mathbf{m}_p, \quad \dot{\boldsymbol{\sigma}}_p = -\dot{\lambda}_p \mathbf{E} : \mathbf{m}_p \tag{3}$$

$$\dot{\boldsymbol{\sigma}}_d = \dot{\lambda}_d \mathbf{m}_d, \quad \dot{\boldsymbol{\epsilon}}_d = -\dot{\lambda}_d \mathbf{E}^{-1} : \mathbf{m}_d \tag{4}$$

where $\dot{\lambda}_p$ and $\dot{\lambda}_d$ are the plastic and the damage multipliers which determine the size of the plastic strain and damage strain increment, respectively, and $\mathbf{m}_p$ and $\mathbf{m}_d$ give the direction of the plastic strain and damage strain increment, respectively. Loading is distinguished from unloading by the Kuhn–Tucker-conditions $F \leqslant 0$, $\dot{\lambda} \geqslant 0$, $F\dot{\lambda} = 0$. From the differential consistency condition

$$\dot{F}_p = \frac{\partial F_p}{\partial \boldsymbol{\epsilon}} : \dot{\boldsymbol{\epsilon}} + \frac{\partial F_p}{\partial \lambda_p} \dot{\lambda}_p = \mathbf{n}_p : \dot{\boldsymbol{\epsilon}} - H_p \dot{\lambda}_p = 0 \tag{5}$$

$$\dot{F}_d = \frac{\partial F_d}{\partial \boldsymbol{\epsilon}_e} : \dot{\boldsymbol{\epsilon}}_{ed} + \frac{\partial F_d}{\partial \lambda_d} \dot{\lambda}_d = \mathbf{n}_d : \dot{\boldsymbol{\epsilon}}_{ed} - H_d \dot{\lambda}_d = 0 \tag{6}$$

the multipliers are gained and set in the flow rule, Eqs. (3) and (4)

$$\dot{\boldsymbol{\epsilon}}_p = \frac{\mathbf{m}_p \otimes \mathbf{n}_p}{H_p} : \dot{\boldsymbol{\epsilon}} = -\mathbf{T}_p : \dot{\boldsymbol{\epsilon}} \tag{7}$$

$$\dot{\boldsymbol{\sigma}}_d = \frac{\mathbf{m}_d \otimes \mathbf{n}_d}{H_d} : \dot{\boldsymbol{\epsilon}}_{ed} = \mathbf{T}_d : \dot{\boldsymbol{\epsilon}}_{ed} \tag{8}$$

where $\mathbf{n}_p$ and $\mathbf{n}_d$ are the normals on the plastic and the damage surface, respectively. If $\mathbf{n} = \mathbf{m}$, we talk about an associated flow rule. Finally, a term for the tangential stiffness is obtained:

$$\mathbf{E}_t = (\mathbf{E} + \mathbf{T}_d) : (\mathbf{I} + \mathbf{T}_p) \tag{9}$$

where $\mathbf{I}$ is the fourth order unity tensor and $\mathbf{T}_p$ and $\mathbf{T}_d$ are explained in Eq. (7) and (8), respectively. The stresses are updated by

$$\boldsymbol{\sigma}^{\nabla} = \mathbf{E}_t : \dot{\boldsymbol{\epsilon}} \tag{10}$$

Now, all equations are established which have to be supplemented by functional relations.

Different failure surfaces for concrete as e.g. the Ottosen Four-Parameter model (see Ottosen, 1977), the Hsieh–Ting–Chen Four-Parameter model (see Hsieh et al., 1982) or the Willam–Warnke Five-Parameter model (see Willam and Warnke, 1975) can be found in the literature (see also Chen, 1994). The form of the failure function is determined by experimental data. The reports by Kupfer et al. (1969) and Tasuji et al. (1964) cover almost the full range of the biaxial stress states. For triaxial stress states, results by Mills and Zimmermann (1970) and Launy and Gachon (1970) are mentioned. According to Schmidt-Hurtienne (2001), the Hsieh–Ting Chen failure surface $F_{d,c}$ for compressive loading is formulated in the strain space and is given by

$$F_{d,c} = c_1 J_2^e + \kappa_{d,c}\left(c_2\sqrt{J_2^e} + c_3 \epsilon_{e,max}^{(\alpha)} + c_4 I_1^e\right) - \kappa_{d,c}^2 = 0 \tag{11}$$

while for tensile loading, $F_{d,t}$ is

$$F_{d,t} = 0.5\boldsymbol{\epsilon}_e^+ : \boldsymbol{\epsilon}_e^+ - 0.5\kappa_{d,t}^2 = 0 \tag{12}$$

where $c_1, \ldots, c_4$ are parameters of the damage surface, I_1^e is the first invariant of the elastic strain tensor $\boldsymbol{\epsilon}_e$, J_2^e the second invariant of $\operatorname{dev}\boldsymbol{\epsilon}_e$, $\epsilon_{e,\max}^{(\alpha)}$ the maximum αth characteristic value of $\boldsymbol{\epsilon}_e$ and $\boldsymbol{\epsilon}_e^+$ the positive projection of the elastic strain tensor, see Eq. (15). The parameters c_1–c_4 are calibrated at standard test so that the biaxial failure surface measured by Kupfer et al. (1969) is reproduced (see Fig. 2). It should be mentioned that we are also able to reproduce triaxial stress states measured by Mills and Zimmermann (1970) as shown in Schmidt-Hurtienne (2001) and Rabczuk (2002). Anisotropic tensile behavior is distinguished from isotropic compressive behavior if the maximum elastic tensile strain is greater than the absolute value of the smallest compressive strain:

$$\left(\boldsymbol{\epsilon}_e^{(\alpha)} \,|\, \max \boldsymbol{\epsilon}_e^{(\alpha)} > |\min \boldsymbol{\epsilon}_e^{(\alpha)}|\right) \rightarrow \text{tension} \tag{13}$$

The plastic surface F_p is based on the positive projection of the elastic strain tensor according to the rule that microcrack-damage develops perpendicular to the direction of the largest principal strain. The plastic surface F_p is

$$F_p = \frac{1}{2}\left(\boldsymbol{\epsilon}_e^+ : \boldsymbol{\epsilon}_e^+ + c_c \boldsymbol{\epsilon}_e^- : \boldsymbol{\epsilon}_e^-\right) - \frac{1}{2}\kappa_p^2 = 0 \tag{14}$$

where c_c is the cross-effect constant (see also Ortiz, 1985) with

$$\boldsymbol{\epsilon}_e^+ = \mathbf{P}^+ : \boldsymbol{\epsilon}_e, \quad \boldsymbol{\epsilon}_e^- = \boldsymbol{\epsilon}_e - \boldsymbol{\epsilon}_e^+ \tag{15}$$

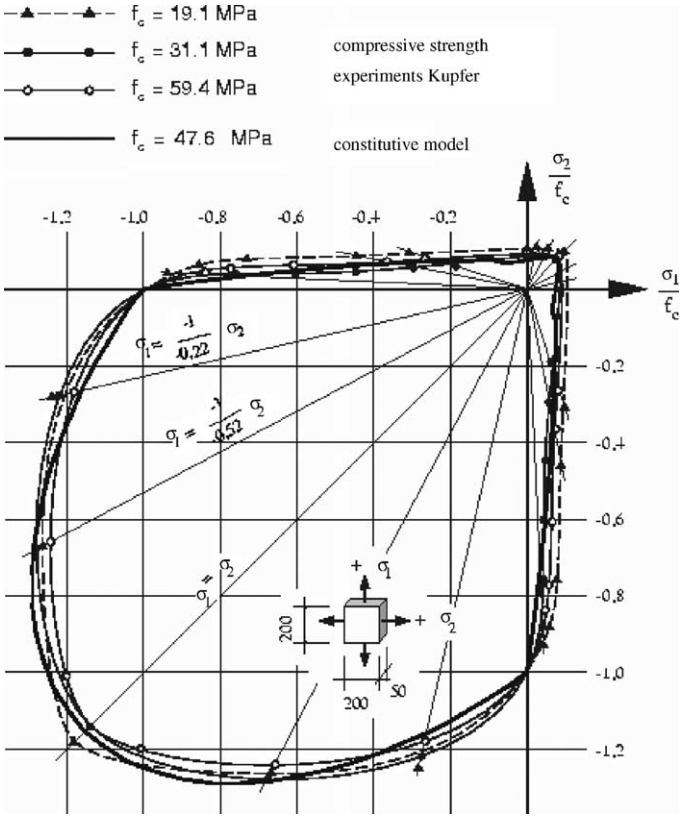

Fig. 2. Biaxial failure surface of concrete.

and

$$\mathbf{P}^{+} = \sum_{\alpha} H(\epsilon^{(\alpha)})\mathbf{d}^{(\alpha)} \otimes \mathbf{d}^{(\alpha)} \otimes \mathbf{d}^{(\alpha)} \otimes \mathbf{d}^{(\alpha)} \tag{16}$$

where H is the heavyside function and $\mathbf{d}^{(\alpha)}$ is the characteristic vector of $\boldsymbol{\epsilon}_{\mathrm{e}}$. For the theoretical maximum of $c_{\mathrm{c}} = 1.0$, we obtain isotropic plasticity (see Fig. 3). For a more realistic value of $c_{\mathrm{c}} = 0.08$, similarities to the failure surface of concrete can be seen as shown in Fig. 3. The damage variable $\widehat{D}$ depends on the equivalent damage strain κ_{d} of the elastic strain tensor. The damage evolution is described by a Weibull distribution:

$$\widehat{D}(\kappa_{\mathrm{d}}) = 1 - \mathrm{e}^{-\left(\frac{\kappa_{\mathrm{d}}-e_0}{e_{\mathrm{d}}}\right)^{g_{\mathrm{d}}}} \quad \kappa_{\mathrm{d}} \geqslant e_0 \quad \text{and} \quad \widehat{D}(\kappa_{\mathrm{d}}) = 0 \kappa_{\mathrm{d}} < e_0 \tag{17}$$

with e_0, e_{d} and g_{d} as material parameters, so that uniaxial compressive and tensile tests are reproduced as shown in Eibl et al. (2001). Zheng (1996) measured the tensile and compressive strengths of pre-damaged concrete specimens. His study showed that the tensile strength of the compression pre-damaged specimen is lower than that of the virgin specimen. The same effect was observed for the compressive strength with tension pre-damage. However, the effect was by far smaller. Especially in wave propagation problems and under cyclic loading conditions, this effect cannot be neglected. To account for this phenomenon, isotropic compressive damage under tensile loading conditions is reduced by a factor r_{c}, so that we were able to reproduce the results obtained by Zheng (1996):

$$D_{\mathrm{c}}^{t+\mathrm{d}t} = \max((\widehat{D}(\kappa_{\mathrm{d,c}}), D_{\mathrm{c}}^{t}) \quad \text{(compression)} \tag{18}$$

$$D_{\mathrm{c}}^{t+\mathrm{d}t} = \max((\widehat{D}(\kappa_{\mathrm{d,c}}/r_{\mathrm{c}}), D_{\mathrm{c}}^{t}) \quad \text{(tension)} \tag{19}$$

where the subscript 'c' indicates compression. The hardening modulus in compression is

$$H_{\mathrm{d,c}} = \frac{\partial F_{\mathrm{d,c}}}{\partial \lambda_{\mathrm{d}}} = \frac{\partial F_{\mathrm{d,c}}}{\partial D_{\mathrm{c}}} = \frac{\partial F_{\mathrm{d,c}}}{\partial \kappa_{\mathrm{d,c}}} \cdot \frac{\partial \kappa_{\mathrm{d,c}}}{\partial D_{\mathrm{c}}} \tag{20}$$

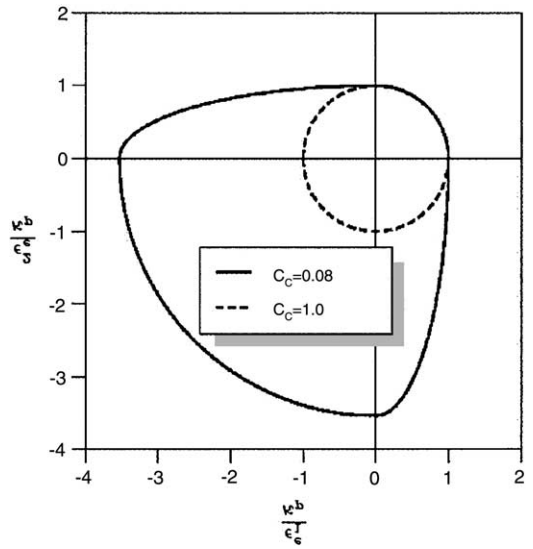

Fig. 3. Plasticity surface of concrete for two different cross constants c_{c}.

The evolution of the anisotropic (tensile) damage tensor $\mathbf{D}_t$ is defined in the direction of the positive principal strain. The damage state is stored in form of a complementary continuity tensor $\mathbf{a}$. Hence, the damage tensor in the direction of the principal strain α is

$$D_t^{t,(\alpha)} = 1 - \mathbf{d}^{(\alpha)} \cdot \mathbf{a} \cdot \mathbf{a} \cdot \mathbf{d}^{(\alpha)} \tag{21}$$

New tensile damage occurs in the direction of the positive principal strain, weighted with a factor r_e to take into account the direction where the maximum damage increases:

$$D_t^{t+\mathrm{d}t,(\alpha)} = \max(\widehat{D}(\kappa_{d,t} \cdot r_e), D_t^{t,(\alpha)}) \quad \text{(tension)} \tag{22}$$

with

$$r_e = \frac{\langle \epsilon_e^{(\alpha)} \rangle}{\max \epsilon_e^{(\alpha)}} \tag{23}$$

where $\langle\ \rangle$ are the McAuly brackets and the subscript 't' indicates tension. According to Eq. (19), tensile damage can occur under compressive loading as well:

$$D_t^{t+\mathrm{d}t,(\alpha)} = \max\left(\widehat{D}(\max[\langle \epsilon^{(\alpha)} \rangle / r_t, \kappa_{d,t}/r_t]), D_t^{t,(\alpha)}\right) \quad \text{(compression)} \tag{24}$$

The reduction factor r_t is far smaller than r_c. The deformation rate for the tensile damage according to Eq. (24) is

$$\dot{\mathbf{D}}_t = \sum_\alpha \dot{D}_t^{(\alpha)} \mathbf{d}^{(\alpha)} \otimes \mathbf{d}^{(\alpha)} \tag{25}$$

The principal direction of the rate of the tensile damage coincides with the one of the elastic strain tensor, but it is not necessarily the case for the total tensile damage tensor, since it depends on the complete loading history. The hardening modulus H_d from Eq. (6) is

$$H_{d,t} = \frac{\partial F_{d,t}}{\partial \lambda_d} = \frac{\partial F_{d,t}}{\partial D_{t,\max}^{(\alpha)}} = \frac{\partial F_{d,t}}{\partial \kappa_{d,t}} \cdot \frac{\partial \kappa_{d,t}}{\partial D_{t,\max}^{(\alpha)}} \tag{26}$$

A detailed derivation can be found in Schmidt-Hurtienne (2001). From Eq. (25), the continuity rate can be computed by

$$\dot{\mathbf{a}} = \sum_\alpha \sqrt{(1 - \dot{D}_t^{(\alpha)})} \mathbf{d}^{(\alpha)} \otimes \mathbf{d}^{(\alpha)} \tag{27}$$

The calculation of the integral of Eq. (27) to obtain the total continuity tensor is not permitted, since under certain circumstances continuities <0, that means damages >1 can occur. Therefore, the continuity tensor $\mathbf{a}$ is computed by

$$\mathbf{a} = \prod_t \mathrm{d}\mathbf{R}_\mathbf{a} \tag{28}$$

with

$$\mathrm{d}\mathbf{R}_\mathbf{a} = \sum_\alpha \frac{a^{t+\mathrm{d}t,(\alpha)}}{a^{t,(\alpha)}} \mathbf{d}^{(\alpha)} \otimes \mathbf{d}^{(\alpha)} = \sum_\alpha \sqrt{\frac{1 - D_t^{t+\mathrm{d}t,(\alpha)}}{1 - D_t^{t,(\alpha)}}} \mathbf{d}^{(\alpha)} \otimes \mathbf{d}^{(\alpha)} \tag{29}$$

Eq. (29) guarantees, that every damage increment in direction of the current principal strain reduces the continuity, but simultaneously the principal values of $\mathbf{a}$ cannot be negative. The relation between the internal plastic variable q_p and the plastic equivalent strain κ_p is described in Eq. (30):

$$q_{\mathrm{p}}(\kappa_{\mathrm{p}}) = c_{\mathrm{p}}(\kappa_{\mathrm{p}} - e_{\mathrm{d}})\left(1 - \mathrm{e}^{-\left(\frac{\kappa_{\mathrm{p}} - e_{\mathrm{d}}}{e_{\mathrm{p1}}}\right)}\right)\mathrm{e}^{-\frac{\kappa_{\mathrm{p}}}{e_{\mathrm{p2}}}} \quad \forall \kappa_{\mathrm{p}} \geqslant e_{\mathrm{d}} \tag{30}$$

with material constants e_{d}, e_{p1}, e_{p2} and c_{p}. Plastic deformations will occur after the initiation of tensile cracks. Since e_{d} corresponds approximately (for $g_{\mathrm{d}} = 1$ exactly) to the strain where the tensile strength in the uniaxial stress–strain curve is reached, the physics are simulated correctly. The parameter c_{p} determines the relation of the internal plastic variable q_{p} to the equivalent plastic strain κ_{p} and must be chosen <1. Otherwise, the plastic strain tensor maybe larger than the total strain tensor. The parameter e_{p1} determines the accumulation and e_{p2} determines the decay of the internal plastic variable at large deformations. As shown in Rots (1988) and Weihe (1995), the decay parameter reduces the shear locking under mixed mode failures. Note that the shear locking effect in meshfree methods is by far smaller than in finite elements. The hardening modulus H_{p} is

$$H_{\mathrm{p}} = -\frac{\partial F_{\mathrm{p}}}{\partial \lambda_{\mathrm{p}}} = -\frac{\partial F_{\mathrm{p}}}{\partial \kappa_{\mathrm{p}}} \cdot \frac{\partial \kappa_{\mathrm{p}}}{\partial q_{\mathrm{p}}} \cdot \frac{\partial q_{\mathrm{p}}}{\partial \lambda_{\mathrm{p}}} = \kappa_{\mathrm{p}} \cdot \frac{\partial \kappa_{\mathrm{p}}}{\partial q_{\mathrm{p}}} \cdot \sqrt{(\boldsymbol{\epsilon}_{\mathrm{e}}^{+} + c_{\mathrm{c}}\boldsymbol{\epsilon}_{\mathrm{e}}^{-}) : (\boldsymbol{\epsilon}_{\mathrm{e}}^{+} + c_{\mathrm{c}}\boldsymbol{\epsilon}_{\mathrm{e}}^{-})} \tag{31}$$

Now, the normals onto the loading surfaces can be computed which are necessary to obtain the tangential stiffness. The normal $\mathbf{n}_{\mathrm{d}}$ of the damage surface is obtained by taking of derivatives F_{d} with respect to the elastic strain tensor $\boldsymbol{\epsilon}_{\mathrm{e}}$ as

$$\mathbf{n}_{\mathrm{d,c}} = \left(c_1 + \frac{\kappa_{\mathrm{d,c}} c_2}{2\sqrt{J_2}}\right)\mathrm{dev}\,\boldsymbol{\epsilon}_{\mathrm{e}} + \kappa_{\mathrm{d,c}}(c_3 \mathbf{d}^{(\alpha)} \otimes \mathbf{d}^{(\alpha)} + c_4 \mathbf{I}) \tag{32}$$

$$\mathbf{n}_{\mathrm{d,t}} = \boldsymbol{\epsilon}_{\mathrm{e}}^{+} \tag{33}$$

The normal of the plastic surface is obtained by derivating F_{p} with respect to the elastic strain tensor:

$$\mathbf{n}_{\mathrm{p}} = \frac{\partial F_{\mathrm{p}}}{\partial \boldsymbol{\epsilon}} = \frac{\partial F_{\mathrm{p}}}{\partial \boldsymbol{\epsilon}_{\mathrm{e}}^{+}} : \frac{\partial \boldsymbol{\epsilon}_{\mathrm{e}}^{+}}{\partial \boldsymbol{\epsilon}} + \frac{\partial F_{\mathrm{p}}}{\partial \boldsymbol{\epsilon}_{\mathrm{e}}^{-}} : \frac{\partial \boldsymbol{\epsilon}_{\mathrm{e}}^{-}}{\partial \boldsymbol{\epsilon}} = \boldsymbol{\epsilon}_{\mathrm{e}}^{+} + c_{\mathrm{c}}\boldsymbol{\epsilon}_{\mathrm{e}}^{-} \tag{34}$$

With the assumption of an associated flow rule, that means $\mathbf{m}_{\mathrm{d}} = \mathbf{n}_{\mathrm{d}}$ and $\mathbf{m}_{\mathrm{p}} = \mathbf{n}_{\mathrm{p}}$, all variables are known for an incremental stress update.

In the transition to the strain softening domain, the sign of the tangential stiffness changes. The type of the partial differential equation (PDE) changes its type from the hyperbolic into eliptic. In this case we talk about a standing wave. The information cannot be propagated any more, which leads to a localization and mesh dependence. As a regularization technique to avoid mesh-dependencies, the static constitutive model is extended with a viscous part, so that the static damage evolution is decayed:

$$\widehat{D}_{\mathrm{total}} = \widehat{D}_{\mathrm{stat}} - \widehat{D}_{\mathrm{dyn}} \tag{35}$$

with

$$\widehat{D}_{\mathrm{dyn}} = \int_{\tau=0}^{t} \frac{\partial \widehat{D}}{\partial \tau} h(t-\tau)\,\mathrm{d}\tau \tag{36}$$

The history function $h(t-\tau)$ can be chosen as an exponential function which decays monotonously from 1 to 0:

$$h(t-\tau) = \mathrm{e}^{-\frac{t-\tau}{\theta}} \tag{37}$$

where τ indicates the time of cracking and θ should be chosen small (<0.07 ms). This technique is able to avoid mesh dependencies as proven by Schmidt-Hurtienne (2001).

Table 1
Material parameters of the constitutive model for concrete

$c_1 = 0.0123424$	$c_2 = 0.025166$	$c_3 = 0.782058$	$c_4 = 0.346384$
$e_0 = 2.5 \times 10^{-5}$	$e_d = 2.2 \times 10^{-4}$	$g_d = 2.5$	$E_0 = 29,000$ MPa
$v = 0.22$	$e_{p1} = 1.1 \times 10^{-3}$	$e_{p2} = 0,4$	$c_p = 0.9$
$c_c = 0.08$	$\varrho = 2.4 \times 10^{-3}$ g/mm^3	$r_c = 20$	$r_t = 1.2$

All material parameters for the simulations are listed in Table 1 where E_0 is the initial elastic modulus, v the poisson ratio and ϱ the density. The parameters are calibrated at standard tests as uniaxial and biaxial compressive and tensile tests, also under cyclic loading (see Eibl et al., 2001), as mentioned above. Note that with this constitutive law and the same parameters (for the corresponding type of concrete) we were able to reproduce a wide range of experiments of concrete structures subjected to quasistatic and dynamic loading, see e.g. Schmidt-Hurtienne (2001) and Rabczuk (2002).

3. The reinforcement

There are several approaches to describe the reinforcement in a numerical analysis. The simplest way is to smear the reinforcement within one element or a certain number of particles, respectively. This procedure does not seem to be appropriate for our interests. Hence, we have chosen to model the reinforcement explicitely, so that an interaction between the reinforcement and the adjacent concrete particles is possible. The reinforcement is discretized with beam elements. As already mentioned, an elastoplastic constitutive law with isotropic hardening and a tension cutoff is applied (see Chen, 1994). Therefore, the tensile stresses are set to zero if the effective plastic strain exceeds a value of $\epsilon_{p,eff} = 0.2$ according to the specifications of the tension wire producer. For the first beam, the yield point of the tension wires is 1470 N/mm^2, the tensile strength is 1670 N/mm^2, the Young's modulus is 200,000 N/mm^2 and the density is 7.8×10^{-3} g/mm^3. For the second beam, the yield point of the tension wires is 1420 N/mm^2, the tensile strength is 1570 N/mm^2. The Young's modulus is 195,000 N/mm^2 and the density is 7.8×10^{-3} g/mm^3.

4. The bond model

Bond models in a numerical analysis are usually proposed at three different scales. At the smallest scale, the 'rib-scale', the geometry of the surface structure of the bar is modeled explicitly. These models are well suited to study the basic behavior of the interface between the concrete and the reinforcement. Because of the high computational effort they are not well suited to model the behavior of a complete reinforced concrete structure.

In 'bar-scale' models, the interface is idealized by a cylindrical shape. The local mechanical interaction at the 'bar-scale' must be accounted for indirectly. The 'bar-scale' models can be classified into two groups, see Cox and Herrmann (1998):

(1) The mechanical interaction is represented by an increased compliance of the concrete matrix adjacent to the bar.
(2) The mechanical interaction is represented by an increased compliance of the concrete-bar interface.

The first approach is simpler, but does not model the wedging effects of the ribs properly. Therefore it is only well suited to capture a pullout failure. The second approach can generally produce both, a pullout and a splitting failure.

The third type of bond model is the so called member scale model. The reinforcement is usually discretized via a discrete, embedded or smeared model, but other novel approaches to model components have also been developed. Typically, at the member scale model, the reinforcement is treated as a one-dimensional element, and bond laws have been limited to single-stress models and are not well suited to reproduce the complicated appropriate bond behavior in certain cases.

As mentioned before, two types of bond failures have to be distinguished, a pullout failure, where the bond strength in the contact zone is exceeded, and a splitting failure which is often caused because of an insufficient concrete cover throughout. Direction changes of the reinforcement promote the latter failure mechanism, too. For our problems, the prestressed concrete beams, where the reinforcement is arranged straight in the concrete, the splitting failure is less significant. A bond model by Akkermann (2001), a simplification of the Den Ujil and Bigaj (1996) model, is adopted. It seems to describe all relevant bond behaviors for our purposes.

The forces are transmitted in the concrete by the ribs of the prestressing. This causes cone-shaped radial cracks in the concrete. In the bond model, an initiation of three radial cracks as shown in Fig. 4 is assumed. The most important parameter is the quotient $\xi = c_{\text{eff}}/D$ of the concrete cover throughout c_{eff} and the diameter D of the rod. If the radial cracks pass through the complete concrete cover throughout, a sudden failure takes place. The bond model is formulated in terms of the radial stress-radial strain relation. This curve can be split into three domains. The first domain describes the nonlinear material behavior caused by the crack propagation, the second domain is the linear softening domain and the third one is characterized by the residual strength.

Domain 1: $0 \leqslant \epsilon_{r,r_s} \leqslant \epsilon_{r,r_{s,\max}}$

$$\sigma_{r,r_s}(\epsilon_{r,r_s}) = \sigma_{r,r_{s,\max}} \frac{k\eta - \eta^2}{1 + (k-2)\eta} \tag{38}$$

with

$$k = \frac{E_r \epsilon_{r,r_{s,\max}}}{\sigma_{r,r_{s,\max}}} \quad \eta = \frac{\epsilon_{r,r_s}}{\epsilon_{r,r_{s,\max}}}$$

and the maximum radial stress $\sigma_{r,r_{s,\max}}$ and strain $\epsilon_{r,r_{s,\max}}$, respectively, at failure (see Akkermann, 2001)

$$\sigma_{r,r_{s,\max}} = 2\xi^{0.88} f_{\text{ct}}, \quad \epsilon_{r,r_{s,\max}} = 4.2\xi^{1.08} \frac{f_{\text{ct}}}{E_0} \tag{39}$$

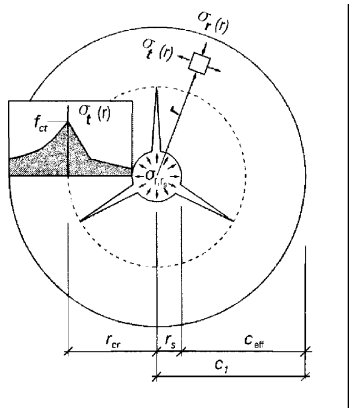

Fig. 4. Bond model with three radial cracks in the concrete.

where E_0 is the Young's modulus, f_{ct} the tensile strength of concrete, $\xi = c_{eff}/D$ where c_{eff} the concrete cover throughout and D the diameter of the rod. The initial stiffness in radial direction is

$$E_r = E_0 \left(\frac{(c_{eff} + D/2)^2 + D^2/4}{(c_{eff} + D/2)^2 - D^2/4} + v \right)^{-1} \tag{40}$$

Domain 2: $\epsilon_{r,r_s,\max} < \epsilon_{r,r_s} \leqslant \epsilon_{r,r_s,\mathrm{res}}$

$$\sigma_{r,r_s}(\epsilon_{r,r_s}) = \sigma_{r,r_s,\max} \left(1 - \frac{1-\psi}{\epsilon_{r,r_s,\mathrm{res}} - \epsilon_{r,r_s,\max}} (\epsilon_{r,r_s} - \epsilon_{r,r_s,\max}) \right), \quad \psi = 0.2 \tag{41}$$

with

$$\epsilon_{r,r_s,\mathrm{res}} = (2\xi + c_0/D)\frac{f_{ct}}{E_0}, \quad c_0 = 0.27m \tag{42}$$

Domain 3: $\epsilon_{r,r_s,\mathrm{res}} < \epsilon_{r,r_s}$

$$\sigma_{r,r_s}(\epsilon_{r,r_s}) = \sigma_{r,r_s,\max} = \psi \sigma_{r,r_s,\mathrm{res}}, \psi = 0.2 \tag{43}$$

The bond stresses and the slip has to be defined parallel to the reinforcement. The transmission of the forces from the reinforcement into the concrete can be considered as shown if Fig. 5. The radial strains can be computed from the slip δ_p by

$$\epsilon_{r,r_s}(\delta_p) = \frac{2\delta_p}{D} \tan \vartheta_b \quad \text{with } \vartheta_b = 0.1 f_c \tag{44}$$

where f_c is the compressive strength of the concrete. The bond stress is coupled with the radial stress by a fictive friction

$$\tau_p = \cot \Phi \sigma_{r,r_s} \tag{45}$$

The friction angle depends on the slope of the circumferential cracks and is approximated by $\cot \Phi = 1$, see Den Ujil and Bigaj (1996). Hence, the bond slip relation is completely determined for a splitting failure. The parameters for the bond model can be found in Table 2.

For a pullout failure, the slip depends on ϑ_b, which decreases with increasing damage of the concrete since the shear resistance of concrete will decrease, too. Finally, the radial strain can be formulated as function of the slip δ_p and the steel strains ϵ_s

$$\epsilon_{r,r_s} = \frac{f(\delta_p, \epsilon_s)}{r_s} \tag{46}$$

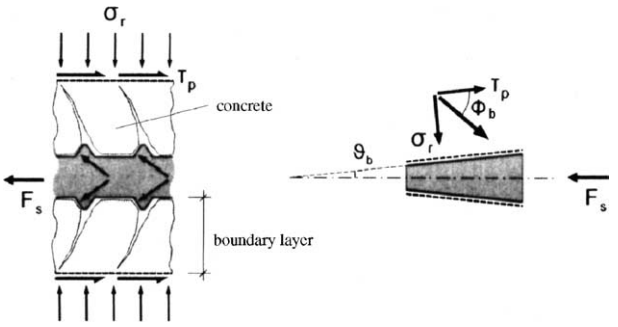

Fig. 5. Bond model.

Table 2
Material parameters of the bond model

	f_{ct} (MPa)	f_c (MPa)	c_{eff} (cm)	D (mm)
Beam I	2.83	−44.5	4.5	7.0
Beam II	2.83	−44.5	3.5	12.0

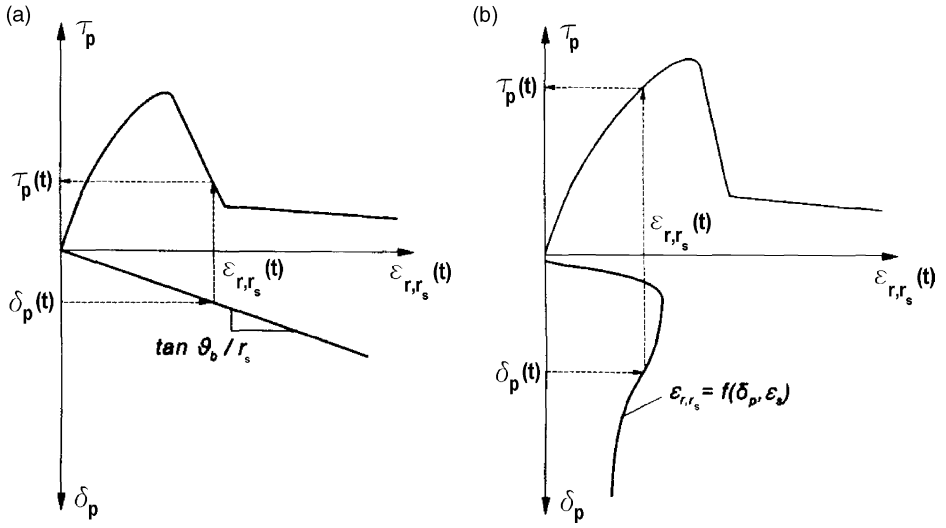

Fig. 6. Bond stress-slip relation for (a) splitting failure, (b) pullout failure.

The function $f(\delta_p, \epsilon_s)$ is divided into four parts. A detailed description can be found in Den Ujil and Bigaj (1996). The bond stresses are computed depending on the relevant failure mechanism. Fig. 6a shows the bond slip relations for a splitting failure, Fig. 6b for a pullout failure. For the splitting failure, $\tan\vartheta_b$ is constant. Hence, the radial strains are linear dependent on the slip. For the pullout failure, the radial strains are nonlinear dependent on the slip. If the radial stresses are smaller than the maximum slip stresses $\sigma_{r,r_s,\max} \leqslant \tau_{p,\max}$ with $\tau_{p,\max} = 5f_{ct}$, a splitting failure takes place, otherwise a pullout failure occurs. The radial strains are calculated according to Eq. (44) or (46) to the corresponding failure mechanism. Once the radial strains are computed, the radial stresses are obtained, which are equal to the bond stresses. The bond stresses are applied to the reinforcement elements and to the adjacent concrete particles. An approach is proposed in Section 5.3 to compute the relative displacements and the slip, and to apply the bond stresses onto the concrete and the reinforcement.

5. Numerical techniques

5.1. The EFG method for modeling the concrete

The EFG method was developed by Belytschko et al. (1994) and frequently applied to crack propagation problems, see Belytschko (1995) and Belytschko and Lu (1995). Usually, the integrals are evaluated by a Gauss quadrature based on a background mesh. A nodal integration was first introduced into EFG by

Beissel and Belytschko (1996) and is similar to the MLSPH method developed by Dilts (1999). The EFG approximation can be written as

$$u_h(\mathbf{x}) = \sum_I \mathbf{p}_I(\mathbf{x})\mathbf{a}(\mathbf{x}) \tag{47}$$

where $\mathbf{p}$ are base functions which are chosen as $\mathbf{p}(\mathbf{x}) = (1 \quad x \quad y)\ \forall \mathbf{x} \in \Re^2$. With the choice of linear base functions, linear completeness is fulfilled, which is desirable since it guarantees the conservation of linear and angular momentum as shown by Belytschko et al. (1998). The constant $\mathbf{a}(\mathbf{x})$ has to be chosen to minimize the functional

$$J = \sum_J \left[\mathbf{p}^{\mathrm{T}}(\mathbf{x}_J)\mathbf{a}(\mathbf{x}) - u_J\right]^2 W(\mathbf{x} - \mathbf{x}_J, h) \tag{48}$$

where W is a weighting function which determines the influence of the central particle $\mathbf{x}$ to its neighborhood, $\mathbf{x}_J$ are the coordinates of the neighbor particles and h is the interpolation radius which determines the size of the domain of influence. Minimizing Eq. (48) with respect to $\mathbf{a}$ leads to the final approximation

$$u_h(\mathbf{x}) = \sum_J \Phi_J u_J \tag{49}$$

which is identical to the finite element interpolation. Since the Kronecker delta property is not fulfilled, Eq. (49) is only an approximation and not a true interpolation as in finite elements. The EFG shape functions are

$$\Phi_J = \mathbf{p}(\mathbf{x})^{\mathrm{T}} \cdot \mathbf{A}(\mathbf{x})^{-1} \cdot \mathbf{p}_J(\mathbf{x}) W(\mathbf{x} - \mathbf{x}_J, h) \tag{50}$$

$$\mathbf{A}(\mathbf{x}) = \sum_J \mathbf{p}_J \mathbf{p}_J^{\mathrm{T}} W(\mathbf{x} - \mathbf{x}_J, h) \tag{51}$$

Crucial is the momentum equation which is given in the weak form by

$$-\int_\Omega \nabla\delta\mathbf{v} : \boldsymbol{\sigma}\,\mathrm{d}\Omega + \int_\Omega \delta\mathbf{v} \cdot (\varrho\mathbf{b} - \varrho\dot{\mathbf{v}})\,\mathrm{d}\Omega + \int_{\Gamma_t} \delta\mathbf{v} \cdot \bar{\boldsymbol{\tau}}\,\mathrm{d}\Gamma = 0 \tag{52}$$

where $\delta\mathbf{v}$ are the test functions and $\mathbf{v}$ are the trial functions, which are identical in a Bubnov Galerkin method. The integrals are evaluated by a nodal integration (see Beissel and Belytschko, 1996)

$$\int_\Omega f(\mathbf{x})\,\mathrm{d}\Omega = \sum_J f(\mathbf{x}_J)\Delta V_J \tag{53}$$

where ΔV_J designates the particle volume.

5.2. A FE beam element to model the reinforcement

The reinforcement is discretized with beam elements. Beam elements are preferred instead of truss elements since truss elements can be loaded only in axial direction and the bond model would have been restricted to one dimension.

5.3. An approach for modeling the bond behavior

The relative displacements $\boldsymbol{\Delta}$ between the reinforcement and the adjacent concrete particles is the starting point for the coupled EFG/FE approach. The relative displacements are

$$\boldsymbol{\Delta} = \mathbf{u}_{\mathrm{fe}} - \mathbf{u}_{\mathrm{mls}} \tag{54}$$

The displacements have to be transformed into one common local coordinate system. Here, we have chosen the local coordinate system of the beam elements. If the beam element is sloped with an angle γ against the x-axis, all necessary particle data has to be transformed with the matrix $\mathbf{T}$ into the local coordinate system:

$$\mathbf{T} = \begin{bmatrix} \cos\gamma & \sin\gamma \\ -\sin\gamma & \cos\gamma \end{bmatrix}$$

After the slip is computed, the bond model can be applied. The traction $\bar{\mathbf{t}}_{\mathrm{b}}$ obtained from the bond model has to be applied onto the FE and the particle domain. Therefore, we have to rotate the traction with the transformation matrix $\mathbf{T}$ back into the global coordinate system. It should be mentioned that in our examples, the beam elements are arranged along the x-axis and since the deformations are very small, the transformation does not have a large influence.

Crucial for the coupling approach is the momentum equation which is given in the strong form by

$$\varrho\ddot{\mathbf{u}} = \nabla\boldsymbol{\sigma} + \varrho\mathbf{b} \tag{55}$$

where ϱ is the density, $\ddot{\mathbf{u}}$ the acceleration, $\boldsymbol{\sigma}$ the Cauchy stress tensor and $\mathbf{b}$ are the body forces. The boundary conditions are

$$\begin{aligned} &\mathbf{n}\cdot\boldsymbol{\sigma} = \bar{\mathbf{t}} \quad \text{on } \Gamma_{\mathrm{t}} \\ &\mathbf{u} = \bar{\mathbf{u}} \quad \text{on } \Gamma_u \\ &\bar{\mathbf{t}}_{\mathrm{b}}^{\mathrm{mls}} = \bar{\mathbf{t}}_{\mathrm{b}}^{\mathrm{fe}} \quad \text{on } \Gamma_{\mathrm{b}} \end{aligned} \tag{56}$$

Γ_{t} and Γ_u are the boundaries either in the particle domain or in the element domain, otherwise the mls and fe superscripts indicate the particle or element domain, respectively. Γ_{b} is a common boundary of the particle and the element domain. On the boundary Γ_{b}, equilibrium between the bond traction is necessary, $\bar{\mathbf{t}}_{\mathrm{b}}^{\mathrm{mls}} = \bar{\mathbf{t}}_{\mathrm{b}}^{\mathrm{fe}}$ as shown in Eq. (56). Including the traction from the bond model, the momentum equation in the weak form can in general be written as

$$\int_\Omega \varrho\delta\mathbf{v}\cdot\ddot{\mathbf{u}}\,\mathrm{d}\Omega + \int_\Omega \nabla\delta\mathbf{v} : \boldsymbol{\sigma}\,\mathrm{d}\Omega - \int_\Omega \varrho\delta\mathbf{v}\cdot\mathbf{b}\,\mathrm{d}\Omega - \int_{\Gamma_{\mathrm{t}}} \delta\mathbf{v}\cdot\bar{\mathbf{t}}\,\mathrm{d}\Gamma \pm \int_{\Gamma_{\mathrm{b}}} \delta\mathbf{v}\cdot\bar{\mathbf{t}}_{\mathrm{b}}\,\mathrm{d}\Gamma = 0 \tag{57}$$

where the last term on the LHS of Eq. (57) has to be added in the particle domain and subtracted in the element domain. Hereby, $\delta\mathbf{v} \in V_0$ are the test functions and $\mathbf{v} \in V_1$ are the trial functions. The spaces V_0 and V_1 are as follows:

$$V_1 = \left(\mathbf{v}|\mathbf{v} \in H^1(\Omega),\ \mathbf{v} = \bar{\mathbf{v}} \text{ on } \Gamma_u\right) \tag{58}$$

$$V_0 = V_1 \bigcap (\delta\mathbf{v}|\delta\mathbf{v} = 0 \text{ on } \Gamma_u) \tag{59}$$

With the test and the trial functions in the particle domain ($\mathbf{x} \in \Omega^{\mathrm{mls}}$)

$$\delta\mathbf{v}^h(\mathbf{x}) = \sum_J \Phi_J^{\mathrm{mls}}(\mathbf{x})\delta\mathbf{v}_J^{\mathrm{mls}} \tag{60}$$

$$\mathbf{v}^h(\mathbf{x},t) = \sum_J \Phi_J^{\mathrm{mls}}(\mathbf{x})\mathbf{v}_J^{\mathrm{mls}}(t) \tag{61}$$

the momentum equation in the weak form can be written as

$$-\int_{\Omega^{\mathrm{mls}}} \nabla \Phi_J^{\mathrm{mls}} \cdot \boldsymbol{\sigma}\,\mathrm{d}\Omega + \int_{\Gamma_{\mathrm{t}}^{\mathrm{mls}}} \Phi_J^{\mathrm{mls}} \bar{\mathbf{t}}\,\mathrm{d}\Gamma + \int_{\Omega^{\mathrm{mls}}} \varrho \Phi_J^{\mathrm{mls}} \mathbf{b}\,\mathrm{d}\Omega + \int_{\Gamma_{\mathrm{b}}} \Phi_J^{\mathrm{mls}} \bar{\mathbf{t}}_{\mathrm{b}}\,\mathrm{d}\Gamma = \sum_I \int_{\Omega^{\mathrm{mls}}} \varrho \Phi_J^{\mathrm{mls}}(\mathbf{x}) \Phi_I^{\mathrm{mls}}(\mathbf{x})\,\mathrm{d}\Omega \frac{\mathrm{d}\mathbf{v}_I}{\mathrm{d}t} \tag{62}$$

For the FE region ($\mathbf{x} \in \Omega^{\mathrm{fe}}$), the momentum equation is

$$-\int_{\Omega^{\mathrm{fe}}} \nabla \Phi_J^{\mathrm{fe}} \cdot \boldsymbol{\sigma}\,\mathrm{d}\Omega + \int_{\Gamma_{\mathrm{t}}^{\mathrm{fe}}} \Phi_J^{\mathrm{fe}} \bar{\mathbf{t}}\,\mathrm{d}\Gamma + \int_{\Omega^{\mathrm{fe}}} \varrho \Phi_J^{\mathrm{fe}} \mathbf{b}\,\mathrm{d}\Omega - \int_{\Gamma_{\mathrm{b}}} \Phi_J^{\mathrm{fe}} \bar{\mathbf{t}}_{\mathrm{b}}\,\mathrm{d}\Gamma = \sum_I \int_{\Omega^{\mathrm{fe}}} \varrho \Phi_J^{\mathrm{fe}}(\mathbf{x}) \Phi_I^{\mathrm{fe}}(\mathbf{x})\,\mathrm{d}\Omega \frac{\mathrm{d}\mathbf{v}_I}{\mathrm{d}t} \tag{63}$$

with

$$\delta \mathbf{v}^h(\mathbf{x}) = \sum_J \Phi_J^{\mathrm{fe}}(\mathbf{x}) \delta \mathbf{v}_J^{\mathrm{fe}} \tag{64}$$

$$\mathbf{v}^h(\mathbf{x}, t) = \sum_J \Phi_J^{\mathrm{fe}}(\mathbf{x}) \mathbf{v}_J^{\mathrm{fe}} \tag{65}$$

Note, that $\Phi^{\mathrm{fe}} = 0\ \forall \mathbf{x} \in \Omega^{\mathrm{mls}}$ and $\Phi^{\mathrm{mls}} = 0\ \forall \mathbf{x} \in \Omega^{\mathrm{fe}}$. The integrals in the particle domain are evaluated by a nodal integration while for the beam elements Gauss point integration is used.

6. Results

6.1. Test setup

We consider two prestressed concrete beams. The first one is of rectangular cross-section. The test setup and the dimensions of the beam are illustrated in Fig. 7. The beam was loaded according to Fig. 7. It was prestressed with two tension wires of 7 mm diameter. The upper one was prestressed with a force of 26.25 KN, the lower one with a force of 11.25 KN. The beam failed in bending because of the plastic flow of the lower reinforcement followed by a failure of the concrete compression zone. Fig. 8 shows a cutout of the beam after the experiment. Crack number 2 and 3 are the cracks which caused the failure. The material parameters for both beams can be found in Section 3.

The test setup for the second beam is similar to the first one and can be found in Fig. 9. In contrast to the first beam, the second one is of I-cross-section. The beam has two tension wires of 12 mm diameter at the

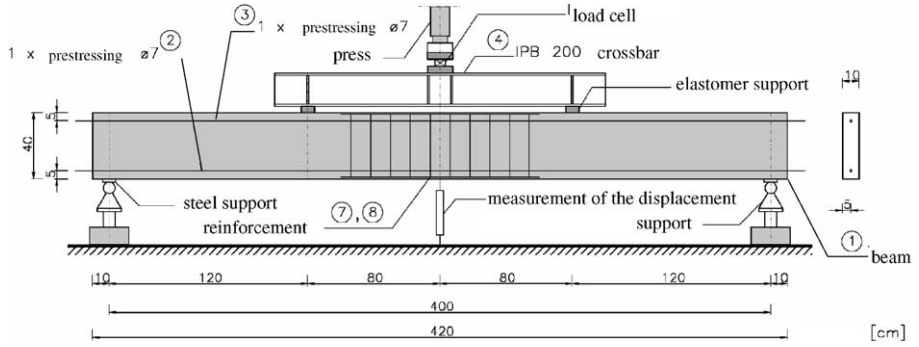

Fig. 7. Test setup of beam I.

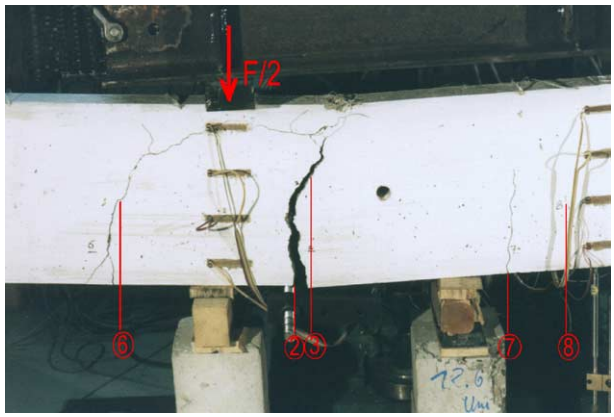

Fig. 8. Beam I after the experiment.

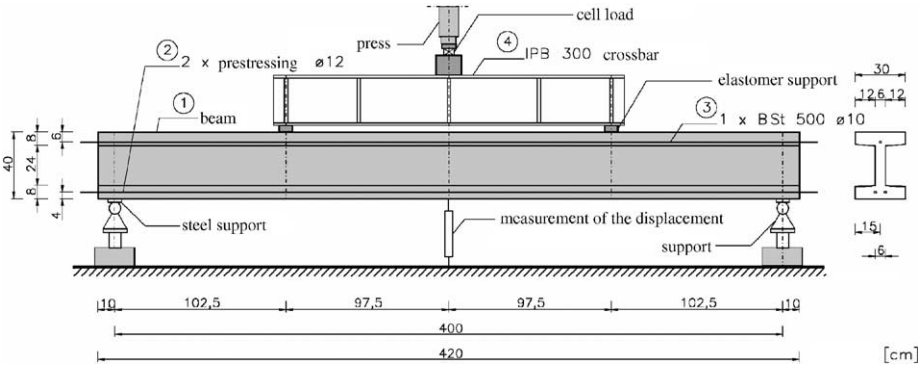

Fig. 9. Test setup of beam II.

lower flange which were prestressed each with a force of 80 KN. The diameter of the upper reinforcement is 10 mm. It was only necessary for the transportation of the beam. The beam failed suddenly because of a combined shear/pullout failure as illustrated in Fig. 10. Crack number 6 caused the failure. It is sloped with 38.6° against the longitudinal axis. At the left hand end of the structure, the pullout failure can be observed. The lower flange was completely destroyed. Finally, it should be mentioned that both beams were loaded by a displacement controlled approach. A detailed description about the experiments can be found in Eibl et al. (2001).

6.2. Comparison of the numerical computation with the experiments

The results are compared in terms of the crack patterns, failure mechanisms and the load mid displacement curves. Both beams are discretized in two dimensions. Plane stress conditions are assumed. The prestressing is modeled via a temperature loading case of the tension wires that the stresses measured in the experiments are obtained. In other words, the tension wire is shortened by cooling down. The strains are computed by $\epsilon = \alpha_t \Delta T$ where α_t is the thermal expansion coefficient which is 1×10^{-5}/C for steel and ΔT is the temperature difference, which is negative in our case. The contraction of the tension wire transmits the prestressing forces in the concrete. In the experiments, we first prestressed the tension wires, then concreted

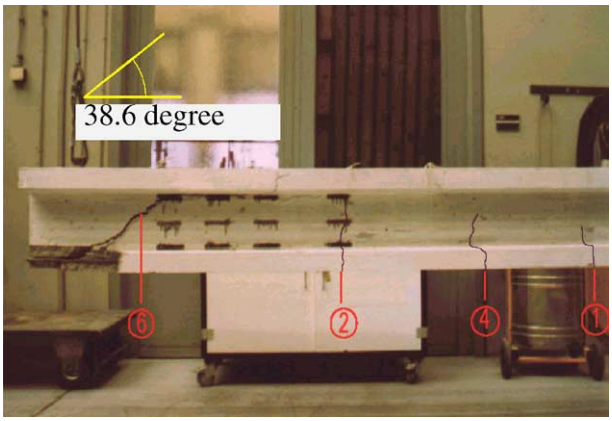

Fig. 10. Beam II after the experiment.

the beams and transmitted the prestressing forces in the concrete after the desired compressive strength ($=44$ N/mm^2) was obtained. Because of the contraction of the concrete, the prestressing forces decreased. To receive the appropriate, i.e. measured, prestressing forces at the time of the experiment, different temperatures were tried out in the numerical simulation. Fig. 11 shows the stresses in the tension wires for beam I in longitudinal direction a short time before the experiment and at the prestressing loading case in the numerical simulation. It can be seen that it takes almost 80 cm in the experiment to transmit the forces into the concrete which is compared to other experiments (see e.g. Idda, 1999 or Eibl et al., 2001) quite large. The transmission length in the computation is 30 cm according to the EUROCODE, 1993 and the experiments by Idda (1999).

Since the topology and load of our beams are symmetrically, we would also obtain a symmetric crack pattern in our computation which does not match well with experimental observations. Therefore, the compressive and tensile strength of the concrete is varied in the beam. We modeled the scatter in strength in the constitutive model by multiplying the stresses in our damage model with a factor α, which scatters around the average of 1.0. According to experimental data (see e.g. Harada and Shinozuka, 1988 and Mirza et al., 1979), a log normal distribution was chosen which scatters as just mentioned around an average of 1

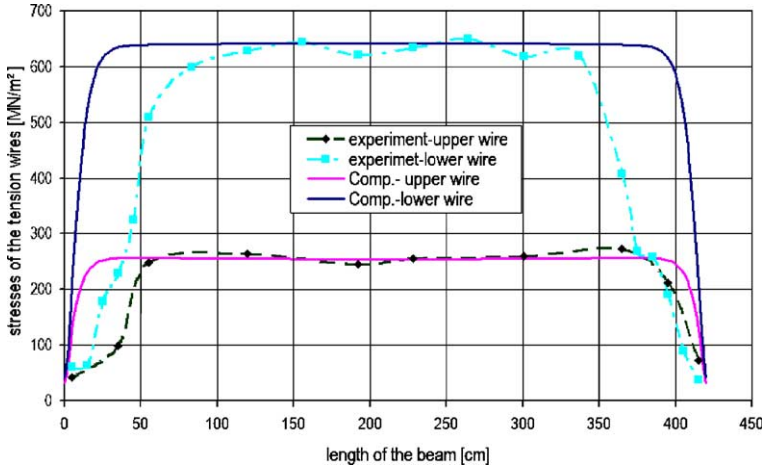

Fig. 11. Stresses in the tension wires for the loading case 'prestressing' of the experiment and the computation.

with a standard deviation of 20%. To produce the random numbers, the NAG library of FORTRAN was used. It has to be mentioned that the results depend on the spatial correlation, but the same effects can be observed in experiments (see e.g. Eibl et al., 2001). Approximately 270,000 particles are used in the analysis. All material parameters for the simulations as well as a detailed description of the numerical models can be found in Eibl et al. (2001).

6.2.1. The bending failure of beam I

Fig. 12 compares the crack pattern of the experiments with the one of the numerical analysis. The calculation produced more cracks than the experiment. The second crack on the left hand side caused the failure in the compressive zone of the concrete in the experiment. The experimental and 'numerical' load displacement curves are illustrated in Fig. 14 and show a good agreement. The computation is stopped before the reinforcement reaches the failure criterion since the calculation is getting unstable. In the experiment, the mid displacement due to failure is smaller than in the calculation. If decreasing the effective plastic strain due to failure for the reinforcement, the curves would coincide better, but we have chosen $\epsilon_{p,eff} = 0.2$ according to the specifications of the tension wire producer. The load displacement curve in the experiment does not begin in the origin because of the prestressing loading case. In view of the large experimental scatter, the computation can reproduce the experimental behavior pretty well.

6.2.2. The shear/anchorage failure of beam II

As mentioned in Section 6.1, the second beam is of I-cross-section. It is also discretized in two dimensions, plane stress. In particle methods, when summing over the neighbor particles, particles from the flange contribute to the sums of particles in the web and vica versa. Because of the large differences in thickness, this might cause errors. We have not done any arrangements, but when choosing the domain of influence as small as possible, errors might be kept small. As we see later, the complete failure mechanism cannot be captured.

Fig. 13 shows the crack pattern of the experiment and the computation. The shear crack in the experiment is closer to the support than in the computation, but a large scatter is observed in the experiments (see Eibl et al., 2001). The shear crack in the experiment has an angle of approximately 38° against the longitudinal axis. The shear crack in the calculation has an angle of 40° against the global x-axis. While in the experiment a combined shear pullout failure is observed, the numerical simulation is able to capture only the shear failure, illustrated by the large damage zone close to the support. The complete failure mechanism

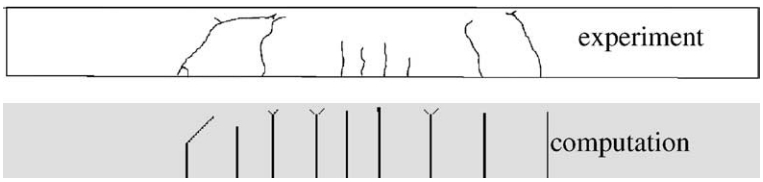

Fig. 12. Comparison of the crack pattern of the experiment with the numerical analysis for beam I.

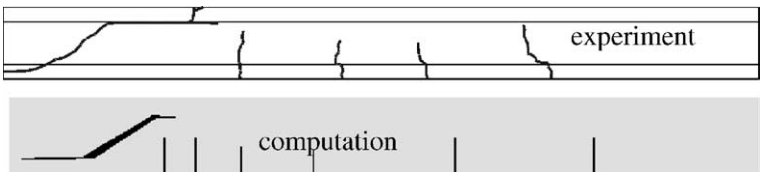

Fig. 13. Comparison of the crack pattern of the experiment with the numerical analysis for beam II.

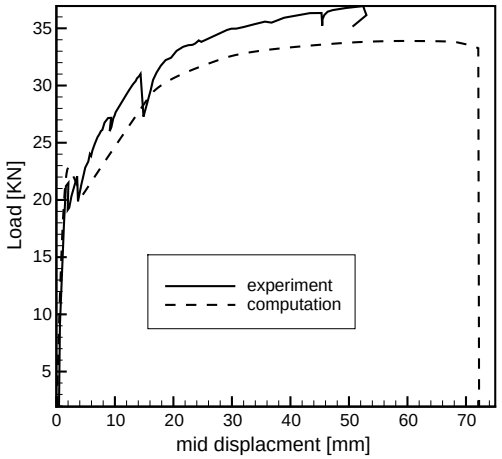

Fig. 14. Load mid displacement curve of beam I.

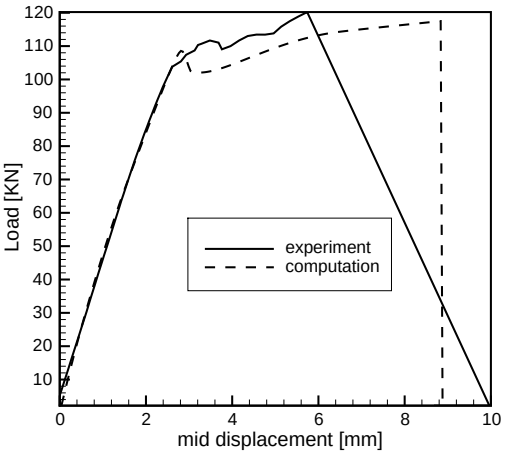

Fig. 15. Load mid displacement curve of beam II.

cannot be reproduced. It might be caused by the large changes in the thickness between the flange and the web. In a 2D (plane stress) analysis, the thickness is assigned to the particles. To capture the complete failure mechanism, a full 3D computation is needed where more particles are necessary to discretize the beam also in the thickness direction. The load displacement curves are compared in Fig. 15 and show a good agreement. The maximum tensile stress of the reinforcement is not reached in the numerical analysis which matches well with the observation in the experiment. Since we are not able to reproduce the pullout failure, the diplacements due to failure are higher in the computation, too. Instead, a crack propagates parallel to the x-axis at the transition between the flange and the web.

7. Conclusions

We have proposed a method for modeling prestressed concrete beams within the framework of a numerical analysis. The concrete is discretized with particles while elements are chosen for the reinforcement.

A continuum based combined damage plasticity model is used for the concrete, but in future, discrete crack models will be applied to benefit from the meshfree character. A bond coupling between particles and elements is proposed so that no interface elements are needed.

The approach is applied to two concrete beams with different failure mechanisms. It is shown that our approach can capture the experimental load displacement curves quite well. Also the crack pattern is reproduced well by the numerical analysis. The model is able to capture different failure mechanisms, a bending failure and a shear failure. For structures of constant thickness, a two dimensional plane stress analysis seems to be sufficient. However, for the second beam, the complete experimental failure, a combined shear/pullout behavior, cannot be reproduced. This might be caused by the two dimensional plane stress assumption. When large changes in thickness occur, a two dimensional model cannot reproduce the appropriate complete failure mechanism. A discrete crack model for the concrete and enhancements in the bond model might improve the results. Meshfree methods are well suited for such kind of problems since boundaries and particles can be added and removed quite easily. A full three dimensional simulation will probably capture the complete failure mechanism. These will be a topic of future investigations.

References

Akkermann, J., 2001. Rotationsverhalten von Stahlbeton Rahmenecken; Dissertation, Institut fuer Massivbau und Baustofftechnologie, Universitaet Karlsruhe.

Beissel, S., Belytschko, T., 1996. Nodal integration on the element-free Galerkin method. Comput. Methods Appl. Mech. Eng. 139, 49–74.

Belytschko, T., Lu, Y.Y., Gu, L., 1994. Element-free Galerkin methods. Int. J. Numer. Methods Eng. 37, 229–256.

Belytschko, T., 1995. Crack propagation by element free Galerkin methods. Eng. Fract. Mech. 51/2, 295–315.

Belytschko, T., Lu, Y.Y., 1995. Element-free Galerkin methods for static and dynamic fracture. Int. J. Solids Struct. 32, 2547–2570.

Belytschko, T., Fleming, M., Organ, D., Krongauz, Y., Liu, W.K., 1996a. Smoothing and accelerated computations in the element free Galerkin method. J. Comput. Appl. Math. 74, 111–126.

Belytschko, T., Krongauz, Y., Organ, D., Krysl, P., 1996b. Meshless methods: an overview and recent developments. Comput. Methods Appl. Mech. Eng. 139, S.3–47.

Belytschko, T., Krongauz, Y., Dolbow, J., Gerlach, C., 1998. On the completeness of Meshfree particle methods. Int. J. Numer. Methods Eng. 43, 785–819.

Chen, W.F., 1994. Constitutive Equations for Engineering Materials, Volume 2: Plasticity and Modeling, Elsevier, Amsterdam, London, New York, Tokyo.

Cox, J.V., Herrmann, L.R., 1998. Development of a plasticity bond model for steel reinforcement. Mech. Cohes-Frict. Mater. 3, 155–180.

Den Ujil, J., Bigaj, A.J., 1996. A bondmodel for ribbed bars based on concrete loaded in compression. Heron 41 (3).

Dilts, G.A., 1999. Moving-least-squares-particle hydrodynamics I: consistency and stability. Int. J. Numer. Meth. Eng. 44, S.1115–1155.

Eibl, J., Stempniewski, L., Rabczuk, T., 2001. Untersuchungen zum Endbereich von im Spannbett vorgefertigten Fertigteiltraegern-Hohlplatten, Abschlussbericht, Institut fuer Massivbau und Baustofftechnologie, Universitaet Karlsruhe.

EUROCODE 2, 1993. Planung von Stahlbeton- und Spannbetontragwerken, Teil 1: Grundlagen und Anwendungsregeln fuer den Hochbau, in Betonkalender 1993, T. II, Ernst und Sohn, Berlin.

Gingold, R.A., Monaghan, J.J., 1977. Smoothed particle hydro-dynamics: theory and applications to non-spherical stars. Mon. Not. R. Astr. Soc. 181, 375–389.

Harada, T., Shinozuka, M., 1988. Scale and Correlation of Stochastic fields, Technical Report, Department of Civil Engineering and Engineering Mechanics, Columbia University, New York.

Hsieh, S.S., Ting, E.C., Chen, W.F., 1982. A plasticity-fracture model for concrete. Int. J. Solids Struct. 18, 181–197.

Idda, K., 1999. Verbundverhalten von Betonrippenstaeben bei Querzug, Dissertation, Institut fuer Massivbau und Baustofftechnologie, Universitaet Karlsruhe.

Kupfer, H., Hilsdorf, H.K., Ruesch, H., 1969. Behavior of concrete under biaxial stresses. ACI, J. 66, 656–666.

Launy, P., Gachon, H., 1970. Strain and Ultimate Strength of Concrete Under Triaxial Stresses, Special Publication, SP-34, ACI, 1, pp. 169–282.

Liang, Q.Q., Xie, Y.M., Steven, G.P., 2001. Generating optimal srut-and-tie models in prestressed concrete beams by performance-based optimazation. ACI Sruct. J. 98 (2), 226–232.

Liang, Q.Q., Uy, B., Steven, G.P., 2002. Performance-based optimization for stut-tie modeling of structural concrete. J. Struct. Eng., ASCE 128 (6), 815–823.

Liu, W.K, Jun, S., Adee, J., Belytschko, T., 1995. Reproducing kernel particle method for structural dynamics. Int. J. Numer. Methods Eng. 38, 1665–1679.

Liu, W.K., Chen, Y., Uras, R.A., Chang, C.T., 1996a. Generalized multiple scale reproducing Kernel particle methods. Comp. Meth. Appl. Mech. Eng. 139, 91–158.

Liu, W.K., Chen, Y., Jun, S., Chen, S., Belytschko, T., Pan, C., Uras, R.A., Chang, C.T., 1996. Overview and applications of the reproducing kernel particle methods, Arch. Comput. Methods Eng., State of the art reviews 3, 3–80.

Lucy, L.B., 1977. A numerical approach to the testing of fission hypothesis. Astr. J. 82, 1013–1024.

Mills, L.L., Zimmermann, R.M., 1970. Compressive strength of plain concrete under multiaxial loading conditions. ACI J. 67 (10), 802–807.

Mirza, S.A., Hatzinikolas, M., Mac Gregor, J.G., 1979. Variability of mechanical properties of reinforced bars. J. Struct. Div. 105, 921–937.

Ortiz, M., 1985. A constitutive theory for the inelastic behavior of concrete. Mech. Mater. 4, 67–93.

Ottosen, N.S., 1977. A failure criterion for concrete. J. Eng. Mech. Div., ASCE 103 (EM4), 527–535.

Rabczuk, T., 2002. Numerische Untersuchungen zum Fragmentierungsverhalten von Beton mit Hilfe der SPH-Methode, Dissertation, Institut fuer Massivbau und Baustofftechnologie, Universitaet Karlsruhe, 2002.

Rots, J.G., 1988. Computational modeling of concrete fracture, PhD thesis, Delft University of Technology.

Schmidt-Hurtienne, B., 2001. Ein dreiaxiales Schaedigungsmodell zur Beschreibung des Dehnrateneffektes von Beton. Dissertation, Institut fuer Massivbau und Baustofftechnologie, Universitaet Karlsruhe.

Tasuji, M.E., Slate, F.O., Tulin, L.G., 1964. Stress–strain relations for concrete under cyclic loading. ACI J. 61 (2), 195–211.

Weihe, S., 1995. Modelle der fiktiven Rissbildung zur Berechnung der Initiierung und Ausbreitung von Rissen- Ein Ansatz zur Klassifizierung, Dissertation, Institut fuer Statik und Dynamik der Luft- und Raumfahrtkonstruktionen Universitaet Stuttgart.

Willam, K.J., Warnke, E.P., 1975. Constitutive Model for the Triaxial Behavior of Concrete, International Association for Bridge and Structural Engineering, Seminar on Concrete Structure Subjected to Triaxial Stresses, Paper III-1, Bergamo, Italy, May 1974, IABSE Proceedings, Vol. 19, pp. 1–30.

Zheng, S., 1996. Beton bei variierender Dehngeschwindigkeit, untersucht mit einer neuen modifizierten Split-Hopkinson-Bar-Technik, Dissertation, Universitaet Karlsruhe, Institut fuer Massivbau und Baustofftechnologie.